Phonon Scattering and Thermal Conductivity in p-Type Nanostructured PbTe-BaTe Bulk Thermoelectric Materials

Shih-Han Lo, Jiaqing He, Kanishka Biswas, Mercouri G. Kanatzidis, and Vinayak P. Dravid**

Transmission electron microscopy studies show that a PbTe-BaTe bulk thermoelectric system represents the coexistence of solid solution and nanoscale BaTe precipitates. The observed significant reduction in the thermal conductivity is attributed to the enhanced phonon scattering by the combination of substitutional point defects in the solid solution and the presence of high spatial density of nanoscale precipitates. In order to differentiate the role of nanoscale precipitates and point defects in reducing lattice thermal conductivity, a modified Callaway model is proposed, which highlights the contribution of point defect scattering due to solid solution in addition to that of other relevant microstructural constituents. Calculations indicate that in addition to a 60% reduction in lattice thermal conductivity by nanostructures, point defects are responsible for about 20% more reduction and the remaining reduction is contributed by the collective of dislocation and strain scattering. These results underscore the need for tailoring integrated length-scales for enhanced heat-carrying phonon scattering in high performance thermoelectrics.

1. Introduction

Increasing global demand for sustainable, renewable and clean energy has rejuvenated research in thermoelectric materials, which have the potential to convert waste heat into usable electricity.[1–3] Studies in this field aim at achieving high figure of merit, *ZT*, to increase thermal energy conversion efficiency. *ZT* is defined as $S^2\sigma T/(\kappa_e + \kappa_l)$, where S is Seebeck coefficient, σ is electrical conductivity, T is absolute temperature, κ_e and κ_l are electrical and lattice thermal conductivities, respectively. Higher energy conversion efficiency is achieved by higher *ZT*.[4] Two obvious approaches to increase *ZT* include: 1) raising the power factor ($\sigma^2 S$)[5] and 2) lowering total thermal conductivity (κ). Reducing lattice thermal conductivity is considered especially effective via enhanced phonon scattering, since increase in power factor constitutes far more complex considerations. In addition, unlike σ, S, and κ_e that are entwined by the carrier concentration (n), κ_l is relatively independent of it.

Enhanced phonon scattering has been achieved in nanoscale structures such as 1D nanowires,[6,7] and bulk samples composed of solid solution or nanoscale precipitates.[8–11] From the practical point of view, bulk materials are more cost-effective and scalable for applications with existing commercial applications, which are mainly in bulk form. It is already known that phonons with mid- to long wavelength can be scattered by nanoscale precipitates while those with shorter wavelengths can be scattered by mass fluctuation in solid solutions.[8,12–15] However, a comprehensive and quantitative understanding of the relationship between microstructure and thermal conductivity has remained elusive.

Recent studies have shown that analysis of the detailed microstructure; comprising interfaces, strain fields, and various defects, by employing advanced transmission electron microscopy (TEM) can shed considerable light on the influence of nanostructuring on lattice thermal conductivity.[15–19] Among all the material systems, PbTe-based nanostructured systems are very promising.[2,20] The host matrix PbTe has the rock-salt structure and good carrier mobility, resulting in favorable combination of higher power factor and nominally lower thermal conductivity. It has been previously shown that introduction of SrTe endotaxial nanostructures further reduces the lattice thermal conductivity of PbTe, but does not significantly degrade the desirable electronic transport properties. The reported *ZT* of nominal PbTe-based nanostructured systems has reached up to 1.8 for n-type ($AgPb_mSbTe_{2+m}$)[8] and 1.7 for p-type (PbTe-SrTe)[12,21] semiconductors at 800 K.

S.-H. Lo, Prof. J. Q. He, Prof. V. P. Dravid
Department of Materials Science and Engineering
Northwestern University
Evanston, IL 60208, USA
E-mail: hejiaqing@mail.xjtu.edu.cn;
v-dravid@northwestern.edu
Prof. J. Q. He
Frontier Institute of Science and Technology (FIST)
Xi'an Jiaotong University
Xi'an 710054, P. R. China
Dr. K. Biswas, Prof. M. G. Kanatzidis
Department of Chemistry
Northwestern University
Evanston, IL 60208, USA
Dr. K. Biswas
New Chemistry Unit
Jawarharlal Nehru Centre for Advanced Scientific Research (JNCASR)
Jakkur, Bangalore 560064, India
Prof. V. P. Dravid
The NUANCE Center
Northwestern University
Evanston, IL 60208, USA

DOI: 10.1002/adfm.201201221

Unlike predominantly coherent endotaxial SrTe nanostructures in PbTe matrix (misfit ≈ 3%), BaTe is expected to exhibit a combination of coherent and semi-coherent PbTe-BaTe interfaces owing to higher lattice mismatch of 0.54 Å with PbTe (misfit ≈ 8%). Thus, depending on the size of precipitates that controls the overall strain energy density, one would expect misfit dislocations in larger precipitates while coherent straining of smaller ones. In order to distinguish the different natures of coherent and semicoherent interfaces in this system, we report detailed microstructure analysis of a series of Na_2Te doped PbTe-BaTe p-type specimens. This system represents the largest lattice mismatch (Table S1, Supporting Information) and potentially highest interfacial dislocation density among several important PbTe-MTe based systems (M = Ca, Sr, Ba).[21] In addition, it is an excellent choice to unravel the nature of solid solution and nanoscale precipitation in PbTe-based nanostructured systems. Such observations would be readily extended to other nanostructured systems which also show a combination of nanostructures embedded in solid-solution matrix comprising high population of point defects.

All of the investigated samples, PbTe-BaTe x% (x = 1, 2, 3, and 4 mole) exhibit nanostructures embedded in solid solution matrix owing to ~0.1% solubility limit of BaTe in PbTe in the measured temperature range. The model of phonon scattering was calculated based on the semi-classical models[14,16,33–39] and the required parameters were retrieved by extensive TEM investigations and the reference.[16] In this study, the solid solution alloy effect is differentiated from that of the nanostructures; and thus the role of point defects on lattice thermal conductivity in the nanostructured bulk systems is specified (Figure S1, Supporting Information). Therefore, the understanding of correlative relationship between microstructure elements and associated phonon scattering is broadened into 0D defects of the nanostructured systems.

2. Results and Discussion

Four samples of 1 mol% Na_2Te doped PbTe- BaTe x% (x = 1, 2, 3, and 4 mole) were synthesized in sealed fused silica ampoules in high-temperature furnaces by stoichiometric reaction of appropriate quantities of PbTe, BaTe, and Na_2Te as described previously.[21] The powder X-ray diffraction (PXRD) patterns (Figure S2, Supporting Information) of PbTe-BaTe samples could be indexed on PbTe structure with an Fm-3m space group; no BaTe or other phase was observed within detection limits of XRD as similar to PbTe-SrTe/CaTe/MgTe system.[12,21,41] Although PXRD pattern is an important tool to prove the existence of BaTe, we have not observed any extra peak due to not only the detection limits of the PXRD but also the presence of very small nanoscale precipitates (size ~ 2 nm) of BaTe in the PbTe matrix. However, a continuous shift of the XRD Bragg peaks towards lower 2θ values with increasing concentration of BaTe was observed. For the cubic system, it implies the expansion of lattice parameter when BaTe (a ≈ 7.001 Å) is added into PbTe (a ≈ 6.46 Å), which also supports that BaTe forms the solid solution with PbTe. More detailed analysis of nanostructures and composition will be presented below by TEM studies and such observations combining PXRD, electron energy loss spectrum (EELS), energy-dispersive x-ray spectrum (EDS) and TEM clearly support a claim of nanostructures embedded in solid-solution matrix comprising high population of point defects.

Temperature dependent electrical and thermal transport properties of these four samples are shown in **Figure 1**. As depicted in Figure 1a, in the measured temperature range, electrical conductivity is decreasing with the increase in the temperature for all samples. It indicates that all the samples are highly doped semiconductor.

The positive Seebeck coefficient shown in Figure 1b in addition to the room temperature Hall measurement (data is not shown) yielding the positive Hall coefficient confirm the p-type carrier. The hole concentration 5.3×10^{19} holes cm^{-3} for PbTe-BaTe 3 mol% sample at room temperature is also estimated in the previous study.[21] Figure 1b,c illustrate that Seebeck coefficient, which drops from the maximum (≈340 μV K^{-1} at 750 K) to ≈75 μV K^{-1} at room temperature, and the power factor, respectively. We should mention here that although all the samples are nominally doped with 1 mol% Na_2Te, the carrier concentration might be varied from sample to sample slightly. For example, in the case of 2 mol% BaTe sample, there might be unexpected loss of Na during the reaction. Therefore, the carrier concentration of this sample is slightly lower comparing to it of others and the lower carrier concentration is also suggested by higher Seebeck coefficient of PbTe-BaTe 2 mol% sample. This is also the reason why it has lower electrical conductivity and lower power factor, resulting in relatively lower *ZT*. However, it is evident that the thermal conductivity shown in Figure 1d decreases with increasing concentration of BaTe. It arises mainly because of the reduction of "lattice" thermal conductivity owing to the rising content of BaTe, and will be discussed in detail below. Figure 1e indicates that samples with higher percentage of BaTe lead to higher *ZT* values (up to 1.3 for 3% BaTe), especially at temperatures above 500 K, which is a useful range for energy conversion efficiency of PbTe-based system at mid-temperature (500–900 K).[22,8] From the discussion of each transport parameter above, it is clear that higher *ZT* value is mainly contributed by the reduction of lattice thermal conductivity, which is highly dependent on the BaTe concentration. There is about a factor of two difference in *ZT* between the samples with high concentration of BaTe (3 and 4%) and low concentration (1 and 2%).

In order to understand the relationship between lattice thermal conductivity and overall microstructure in the Na_2Te doped PbTe-BaTe samples, an analysis of individual microstructural elements was carried out by scanning transmission and conventional TEM (S/TEM). It reveals that high number density nanostructures are present in the samples. The correlation of size and density of nanoscale precipitates with the percentage of BaTe is shown in **Figure 2**. The low-magnification images (Figure 2a,b) depict the samples containing 3 and 1 mol% BaTe, respectively. Many dark-contrast spherical precipitates with nominal size of less than 20 nm are observed. Corresponding electron diffraction pattern (DP) along [011] zone axis (inset) with an aperture including matrix and several precipitates shows only one set of Bragg reflections. There is no differentiation between the matrix and precipitate phases in the diffraction pattern owing to the low proportion of nanoscale precipitates/matrix in the selected area and small lattice

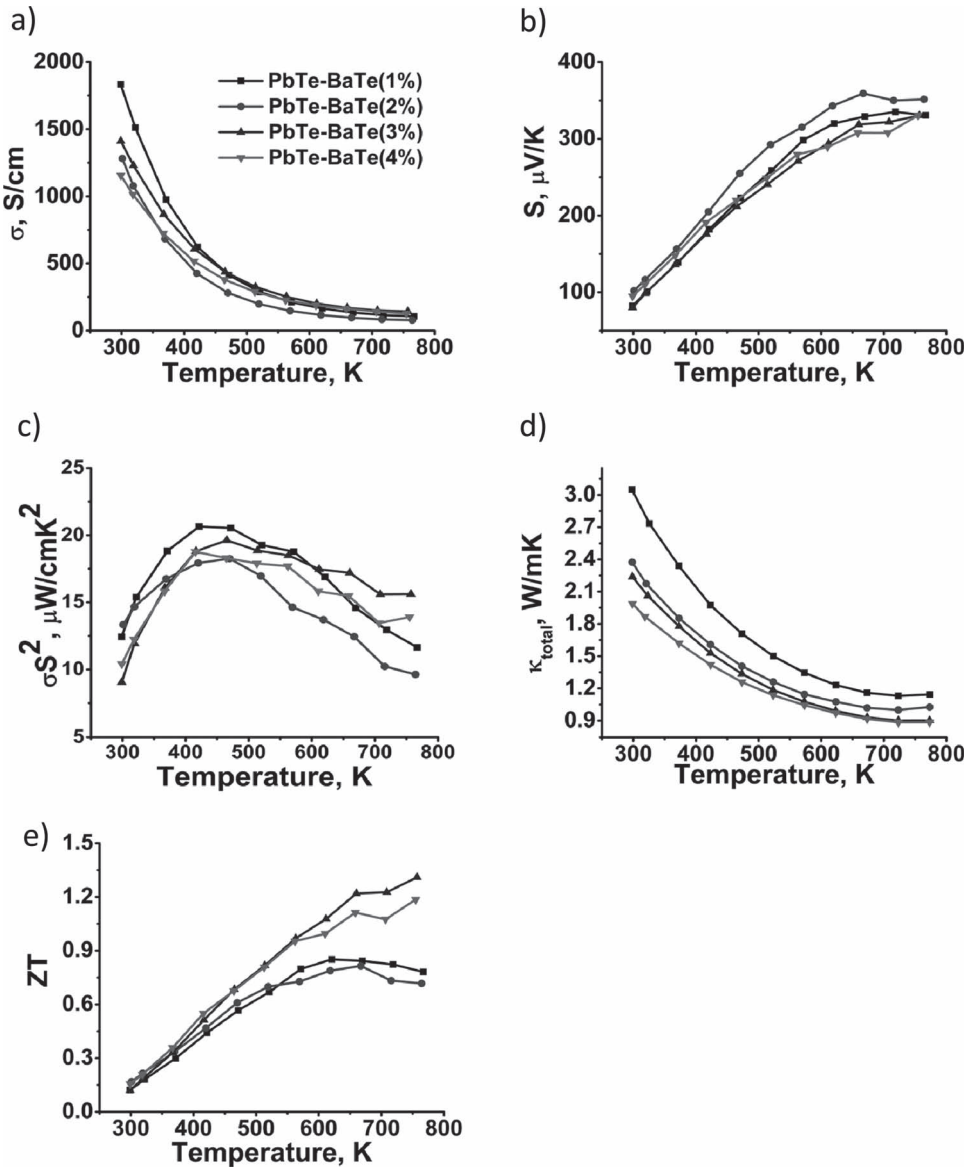

Figure 1. Temperature dependence of electrical and thermal transport properties of PbTe-BaTe doped with 1 mol% Na_2Te. a) Electrical conductivity (σ), b) Seebeck coefficient (S), c) power factor (PF), d) total thermal conductivity (κ_{Total}), and e) thermoelectric figure of merit (ZT).

mismatch. However, the DP including only one big precipitate (≈700 nm) and small portion of the matrix is shown in Figure S3 (Supporting Information) and the corresponding d-spacing is marked for BaTe and PbTe.

To further confirm the size and number density distribution in typical samples, we performed statistical analysis, shown in Figure 2c. From the histogram of approximately the same volume for two samples, we find that the size of precipitates is in the range of 2 to 15 nm and it is obvious that 3% BaTe sample has higher number density than that of 1% BaTe sample. Although it is challenging to quantitatively confirm the composition of these nanostructured systems because of the difficulty in differentiating the matrix and the precipitate signals, EELS (Figure 2d) and EDS (Figure 2e) measurements were conducted to confirm the existence of Ba and Te in the large precipitates. In the EELS patterns, the Ba M4, 5 edges are clearly seen when the beam was positioned at the spot 2 (precipitate) while there is no Ba signal at the spot 1 (matrix). In order to enhance the visibility of the core-loss edges of Ba, the background signals, which originate from multiple scattering, need to be subtracted. Fourier-ratio plural scattering removal method was thus conducted to deconvolute the core-loss spectrum and the zero-loss spectrum, which is obtained as a reference of plural scattering, of respective spots.[23] The similar backgrounds shown in Figure 2d indicate that these two spots have comparable thickness.

To get additional compositional information, two samples (PbTe-BaTe 3%-Na_2Te 1% and PbTe-BaTe 7%) were also

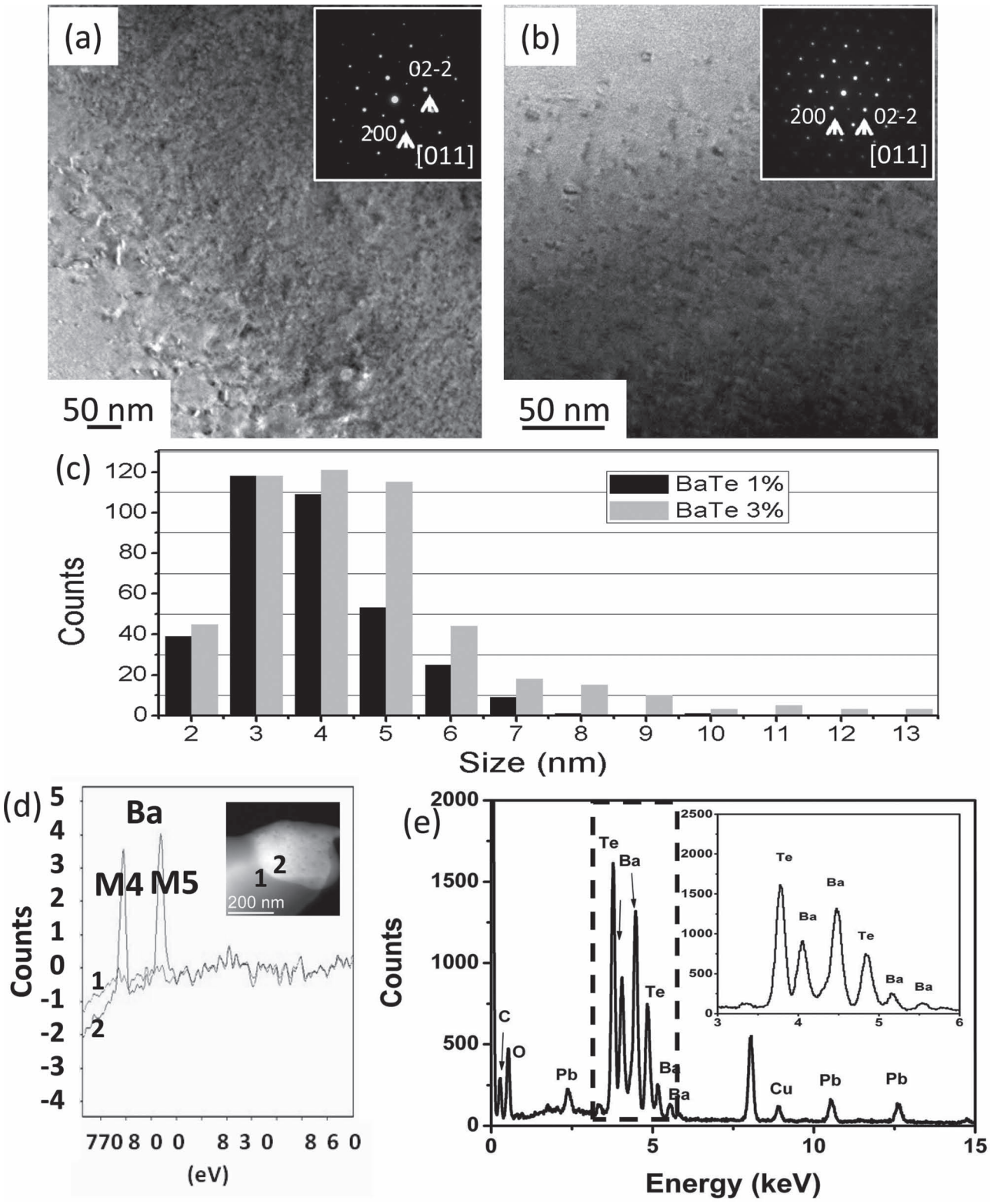

Figure 2. TEM analysis of PbTe-BaTe doped with 1 mol% Na_2Te. Low-magnification TEM images of PbTe containing 3 mol% (a) and 1 mol% of BaTe (b). The insets in the (a) and (b) show the corresponding electron diffraction patterns. c) Histogram of BaTe nanoscale precipitate size distribution and d,e) EELS and EDS spectra confirming the element Ba.

investigated by atom probe tomography (APT) with a commercial Local Electrode Atom Probe (LEAP) instrument.[24,25] Interestingly, APT shows that in fact BaTe may be completely soluble in PbTe when x% BaTe in PbTe is less than 0.5% at room temperature, i.e., formation of solid solution $Pb_{1-x}Ba_xTe$ ($x < 0.5\%$). Due to the localized observation of APT and inhomogeneous

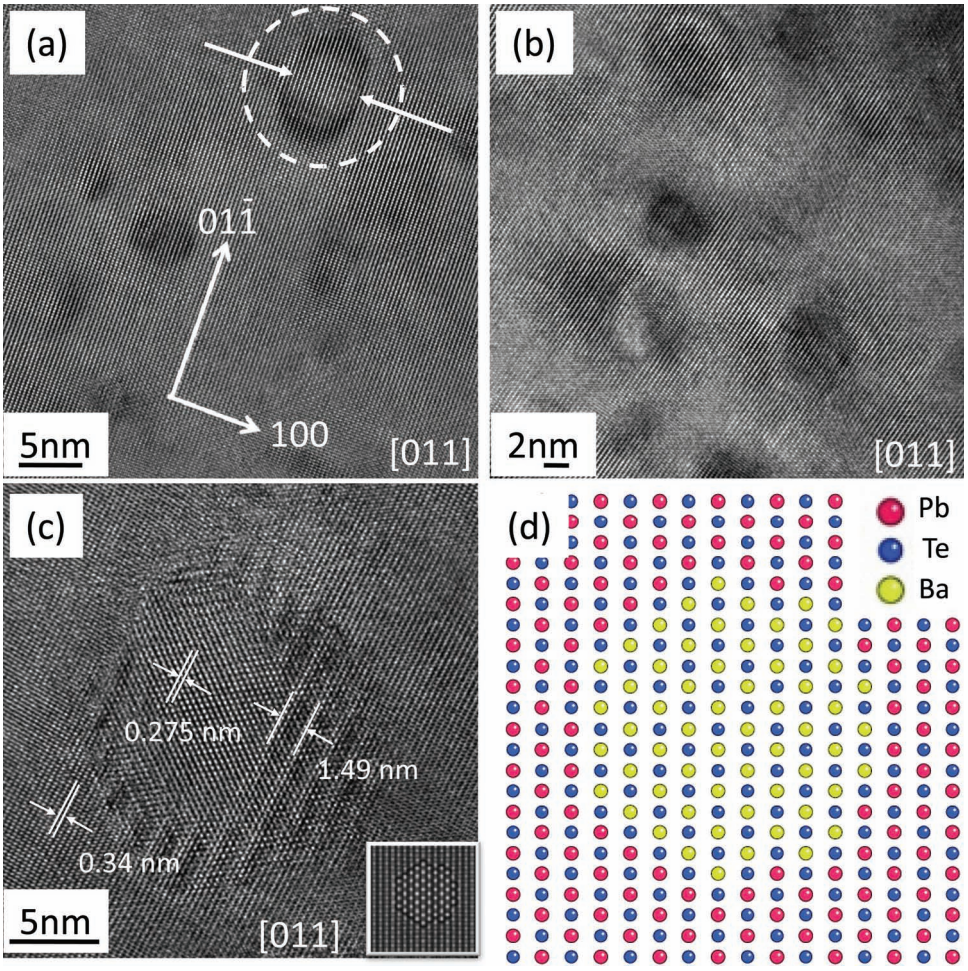

Figure 3. High-resolution TEM phase contrast images of the precipitates and atomic model. The BaTe nanoscale precipitates embedded in PbTe matrix with coherent interface, for 3 mol% BaTe (a) and 1 mol% BaTe (b). Enlarged high-resolution TEM phase contrast image of precipitate with modulation (c), and correspondingly, the simulated image in the inset and the atomic model (d).

nature of the samples, it leads to different values of solubility at different observed spots. However, when x% value is greater than the solubility limit, the extra BaTe mainly forms nanostructures as shown in Figure 2a,b. Detailed APT studies will be published elsewhere. It should be mentioned here that we assume a similar solubility limit in the measured temperature range based on the S/TEM studies of rapid cooling (water and air quenched) processed samples (see Figure S4, Supporting Information). There are no significant variances of nanostructure morphologies and number density between samples prepared by different quenched rates. In addition, the measured temperature is only about a quarter of BaTe melting point. It is not expected that solubility would change significantly in this measured temperature range. Therefore, our calculation (below) based on the TEM observation should be valid under the 10% error range for the property measurement.

High-resolution TEM images of **Figure 3**a,b show the case of the coherent interface between the nanoscale precipitates and the matrix.[21,26] In the case of coherent spherical nanoscale precipitates, the dark contrast mostly resembles to the Ashby-Brown strain contrast.[27,28] Ashby-Brown contrast is a special case of the strain-field contrast dedicated to the description of coherent, spherically symmetrical strain. A typical case is circled in Figure 3a. The line with no contrast is marked by arrows corresponding to the plane that is not distorted by the strain field of the precipitates. The simplified atomic model and simulated images of the precipitate and the matrix assuming the full strained and high coherence between PbTe and BaTe are illustrated in Figure 3d and the corresponding high resolution image is shown in Figure 3c. The Moiré fringes can be found around the precipitate. It is well known that Moiré fringes are formed by the interference between two sets of planes with nearly common periodicity and small relative rotation angle. The correlation between two interfaces can be determined by measuring the spacing of the lattice as indicated in Figure 3c and applying the general Moiré fringes relationship[29] given by:

$$d_{gm} = \frac{d_1 d_2}{\sqrt{(d_1 - d_2)^2 + d_1 d_2 \beta^2}} \quad (1)$$

d_{gm} (≈1.49 nm) is the spacing of the fringes, d_1 (≈0.34 nm) and d_2 (≈0.28 nm) are the lattice spacing of the matrix and the

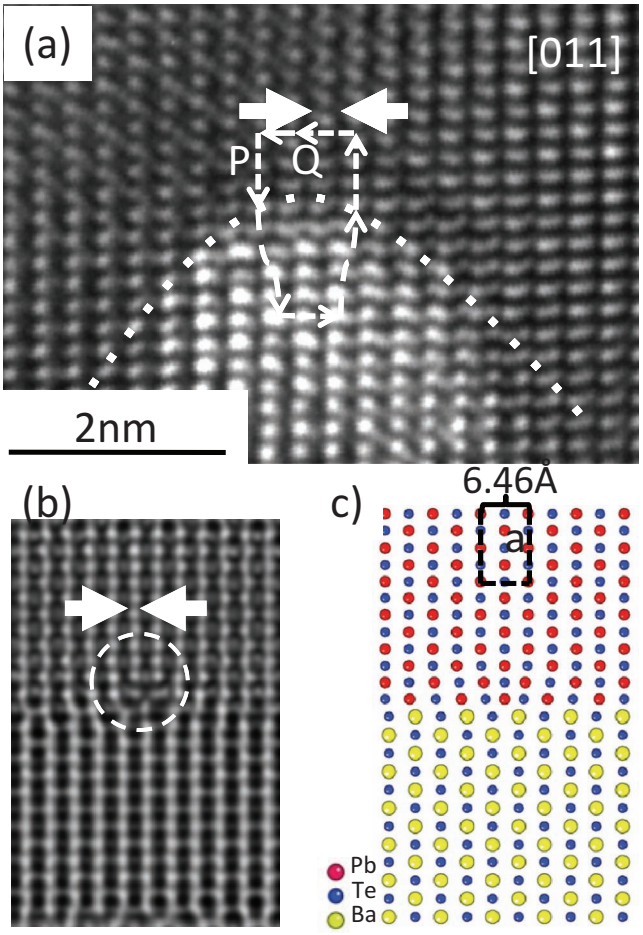

Figure 4. High-resolution TEM phase contrast image of the dislocation and the atomic structural model. a) The high-resolution image of the misfit dislocation on the boundary between the matrix and the precipitate. The dislocation is circled in the simulated image as b) and the extra plane is indicated by arrows. c) The corresponding atomic structural model of the boundary and the misfit dislocation.

precipitate along [100], respectively, and β is the relative rotation angle. The spacing periodicity and rotation angle are cross-checked by the Equation (1) and confirm that the small rotation angle between (220) planes of PbTe matrix and BaTe precipitate is about 1.26°. Detailed analysis of the boundaries between the precipitates and matrix is shown in **Figure 4** and **Figure 5**. The defect, i.e., the misfit dislocation, is observed at the interface in the high resolution TEM phase contrast image as shown in Figure 4a. The extra lattice plane is located at the side of PbTe, which has smaller lattice parameter (a = 0.646 nm) than that of BaTe (a = 0.7001 nm). The dotted line differentiates two phases of the matrix and the precipitate.

Figure 4b and 4c represent the simulated image along [110] zone axis and the modeling of the misfit dislocation. The dislocation core is circled. This model demonstrates the measured displacement vector of $\frac{a}{2}[100]$. In addition, the strain field, caused by the lattice mismatch between PbTe and BaTe, around the boundaries was semi-quantitatively measured by geometric phase analysis (GPA) technique.[30,31] The high quality and clear lattice image with several precipitates marked as "i", "iv" and "v" is shown in Figure 5a. Figure 5b shows a power spectrum image of Figure 5a, which was obtained from Fourier mask filtering image processing. Comparing this diffractogram obtained by fast Fourier transform (FFT) with the DP shown in Figure 2, we can see two sets of superimposed DPs. One set is exactly the same as the DP along [110] zone axis (insets in Figure 2a,b) and another set is the diffuse spot indicated by white triangles. These superlattice-like spots, which appear due to the multiple-scattering, were selected to reconstruct the inverse fast Fourier transform (IFFT) image as depicted in Figure 5c. Modulation due to the crystal defect and overlapping of the matrix and the precipitate, which are both not edge-on here, can be clearly seen here for the stacking faults "ii" and precipitate "i", respectively. Modulation is not a special case but can be found easily among the matrix/precipitate interfaces, as Moiré fringes in Figure 3c being another example.

Figure 5d,e show the tensile in-plane strain field ε_{yy} and ε_{xx} (indicated as y and x in Figure 5a), respectively. The strain field is calculated based on the high resolution lattice image. Both elastic as well as plastic strains are observed here. The elastic strain occurs around the precipitate "i" with about 5% lattice mismatch. The crystal defect, which is stacking faults here and can be seen as two partial dislocations marked as "ii" and "iii", exhibit the plastic strain in the system.

Figure 6a illustrates the lattice thermal conductivity. The lattice thermal conductivity (κ_l) is assessed by subtracting the electrical thermal conductivity (κ_e) from the total thermal conductivity (Figure 1e) and κ_e is obtained by Wiedemann-Franz law. Lorentz number, L, is calculated based on our experimental thermopower data as described previously.[19]

To understand the mechanisms of phonon scattering in this PbTe-based system, semiclassical theoretical calculation based on the modified Callaway's model[32] is conducted. According to the Callaway's model the lattice thermal conductivity is expressed as

$$\kappa_1 = \frac{k_B}{2\pi^2 c}\left(\frac{k_B T}{\hbar}\right)^3 \int_0^{\frac{\theta_D}{T}} \tau_c \frac{e^x}{(e^x-1)^2} x^4 \mathrm{d}x \quad (2)$$

Where x is defined as $\hbar\omega/k_B T$, k_B is the Boltzmann's constant, $\hbar$ is Plank constant, c is an average phonon-group velocity, T is absolute temperature and θ_D is Debye temperature. Based on TEM studies, the τ_c is the combined term, which relates the scattering from Umklapp process, normal processes, dislocations, precipitates, strains, and point defects, respectively by the equation:

$$\tau_c^{-1} = \tau_U^{-1} + \tau_N^{-1} + \tau_D^{-1} + \tau_P^{-1} + \tau_S^{-1} + \tau_{PD}^{-1} \quad (3)$$

Relaxation time due to Umklapp and normal processes are acquired based on the fitting of the experimental thermal conductivity data.[33,34] On the other hand, τ_D is estimated based on the equation provided by Zou et al.,[35] assuming the occurrence of only edge dislocations and greater dependence on the dislocation number density here. Moreover, density and size of nanoparticles play important roles when calculating τ_P[36,37] as well as when considering elastic strain field effect that are

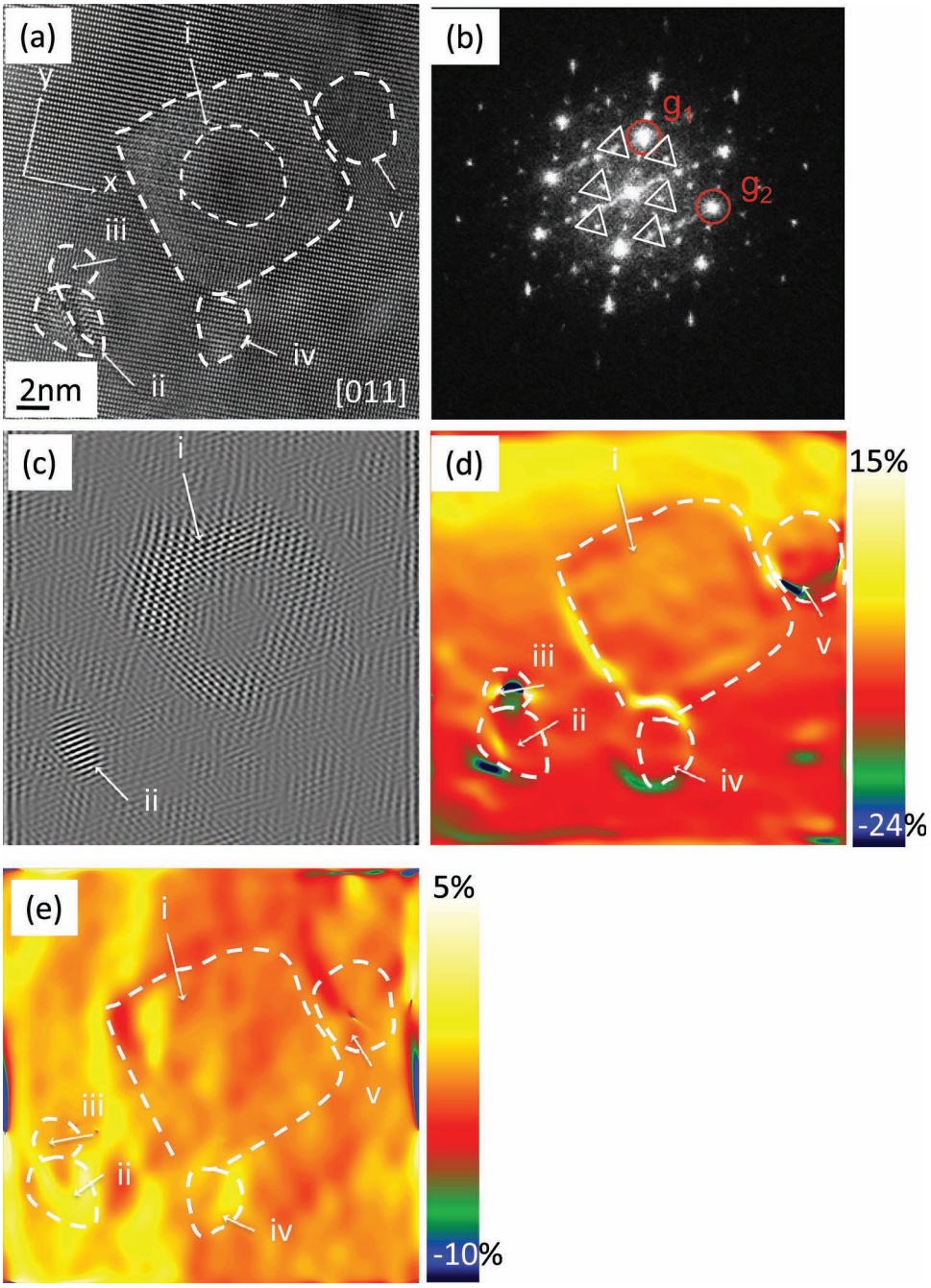

Figure 5. Strain analysis of PbTe-BaTe. a) High-resolution TEM phase contrast image of nanoscale precipitates and stacking faults. b) The corresponding power spectrum is composed of two sets of pattern, one is [200] as g_1 and [02-2] as g_2 indicated by red circles and another is white triangles. c) The inverse fast Fourier transform image showing the coherent interface and modulation around the precipitate i and stacking faults ii. d,e) The shear strain distribution of the nanoscale precipitates along y and x directions. There are elastic strains around the precipitate marked as i and the plastic strain are observed at the dislocation core indicated as ii, iii.

adopted here. Strain field is also taken into account using the model provided in reference [38]. The last term, τ_{PD}, describing the contribution of point defects from solid solution part, is given by:[39]

$$\tau_{PD}^{-1} = A\Gamma = \frac{\omega^4 \delta^3}{4\pi \upsilon^3}\Gamma \tag{4}$$

$$\Gamma = \Gamma_S + \Gamma_M \tag{5}$$

In the above equation, δ is the radius of the impurity atom in the host lattice, υ is the average lattice sound velocity and Γ is the disorder scaling parameter, which depends on mass and strain field fluctuations. Both types of fluctuations are taken to have an additive effect on Γ.[40] The mass fluctuations are quantified by Γ_M that takes into account the average mass of

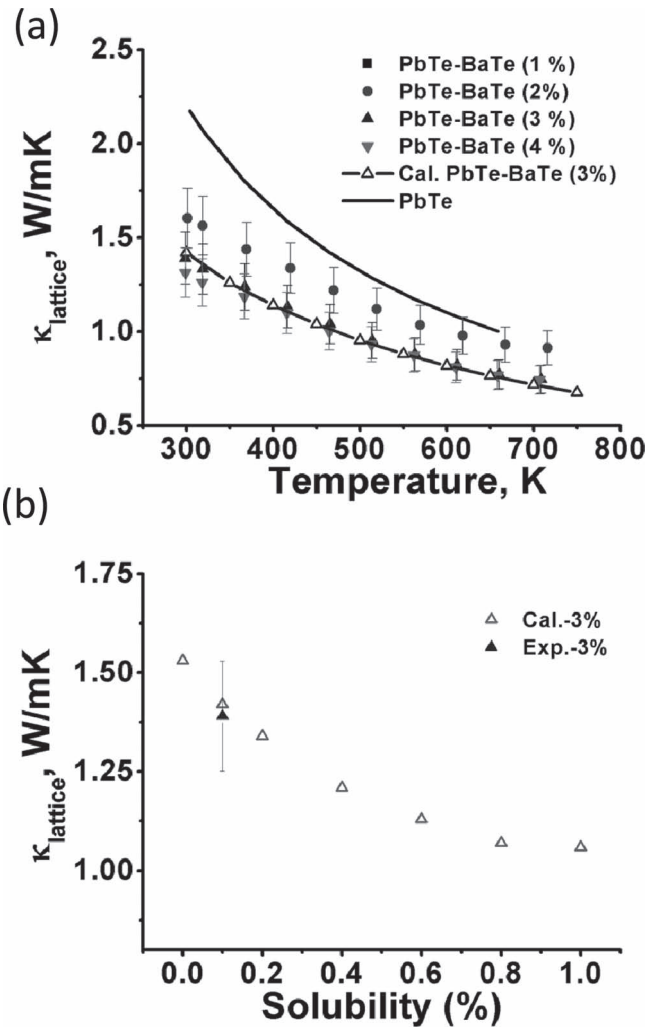

Figure 6. Lattice thermal conductivity. a) Experimental (scattered symbol with 10% error margin) and calculated (open symbol) data of temperature depended lattice thermal conductivity. b) Solubility dependence on lattice thermal conductivity of 3 mol% BaTe sample.

each sublattices and by the strain field fluctuations, Γ_S, that is a value weighted by the average sublattice mass, the average sublattice ionic radius and a phenomenological parameter ε.[14] The parameter ε is a function of the Grüneisen parameter and hence is a measure of the anharmonic contributions to the lattice.[39] The explicit relations of Γ_M and Γ_S are given by Yang et al.[41] as:

$$\Gamma_M = \frac{\sum_{i=1}^{n} c_i \left(\frac{<M_i>}{M^*}\right)^2 f_i^1 f_i^2 \left(\frac{M_i^* - M_i^*}{<M_i>}\right)^2}{\sum_{i=1}^{n} c_i} \quad (6)$$

$$\Gamma_S = \frac{\sum_{i=1}^{n} c_i \left(\frac{<M_i>}{M^*}\right)^2 f_i^1 f_i^2 \varepsilon \left(\frac{r_i^1 - r_i^2}{<r_i>}\right)^2}{\sum_{i=1}^{n} c_i} \quad (7)$$

where the symbols in Equation (6) and (7) are as following: c_i is the degeneracy (here $c_1 = c_2 = 1$), f_i is the fractional occupation, $<r_i>$ is the average radius, $<M_i>$ is the average mass of each sublattice and M^* is the average atomic mass of the compound. To estimate the solid solution $Pb_{1-x}Ba_xTe$ composition, we calculated the mol% of BaTe nanoscale precipitates based on the average size and number density retrieved by the TEM study. Solubility x is in the range of 0.001 to 0.013 resulting from the disparity between calculated BaTe mol% and the nominal composition. To illustrate the significance of the point defects effect, Figure 6b demonstrates that lattice thermal conductivity decreases with increasing solubility of Ba. The range of solubility is given instead of an exact number because it is difficult to measure the average solubility of the whole specimen by the localized TEM observations.

Based on these formulae and most of the parameters from TEM observations (**Table 1**) and the reference,[16] the relaxation time of each scattering process is calculated and results in the lattice thermal conductivity of the sample containing 3 mol% BaTe. **Figure 7** shows the corresponding frequency-depended relaxation times of each phonon scattering mechanism at room temperature. It indicates that point defects as well as dislocations scatter phonons with high frequency, while nanoscale precipitates play an important role in phonon scattering at low frequency. Phonons with medium frequency are scattered by strain. In order to compare the reliability of the calculations, we directly compare the lattice thermal conductivity of our calculated values to experimentally derived values, as plotted in Figure 6a. The calculated result fits to the experimental measured data within the 10% error margin. This indicates strong evidence that the proposed model is consistent between theoretically and experimentally derived parameters for this nanostructured system.

3. Conclusion

In summary, a detailed investigation of PbTe-BaTe nanostructured system using advanced S/TEM shows the close relationship between the microstructure and thermoelectric figure of merit, specifically by virtue of the lattice thermal conductivity. The model of phonon scattering is built to reveal the contribution from various microstructure elements. Unlike previous reports of PbTe-MTe nanostructured bulk systems, the present study differentiates the point defect from the other microstructure constituents. Other than the boundaries, dislocations, strain and nanoscale precipitates, of which size and number density can be manipulated by controlling the nominal composition, point defects also play an important role in reducing the lattice thermal conductivity. In this studied system, a range of solubility is estimated and 0.1% solubility appears responsible for about 20% reduction in the lattice thermal conductivity. Thus, the solid solution nature of nanostructured systems is important in contributing to reduction in lattice thermal conductivity, and must be taken into account for further advances in high performance bulk thermoelectrics.

4. Experimental Section

Nominal PbTe-BaTe (1 to 4 mol%) doped with Na_2Te (1 mol%) samples were prepared in an ingot form at the scale of 10 g. Starting with mixture of high purity Pb, Te, Ba and Na_2Te with appropriate ratios in an evacuated carbon-coated quartz tube, the heating profile was then

Table 1. Input parameters for calculation of relaxation time of phonon scattering for PbTe –3 mol% BaTe.

Relaxation time	Parameter	Symbol [unit]	Value
$\tau_U^{-1} \approx \frac{\hbar\gamma^2}{M\upsilon^2\theta_D}\omega^2 T \exp(-\theta_D/3T)$	Grüneisen parameter of PbTe	Υ	1.96
	Average sound velocity of PbTe	υ [m/s]	1770
	Debye temperature of PbTe	θ_D [K]	136
	Average mass of an atom of PbTe	M [kg]	2.7767×10^{-25}
$\tau^{-1}{}_N \approx \beta\tau_U^{-1}$	Ratio of normal phonon scattering to Umklapp scattering	β	2.5
$\tau_D^{-1} \approx \eta_D N_d \frac{V_0^{4/3}}{2}\omega^3$	Dislocation density	N_d [m^{-2}]	4×10^{15}
	Volume per atom for PbTe	V_0 [Å^3]	33.69
$+ \frac{2^{3/2}}{3^{7/2}}\eta_D N_d B_d^2\gamma^2\omega\left\{\frac{1}{2}+\frac{1}{24}\left(\frac{1-2\nu}{1-\nu}\right)^2\left[1+\sqrt{2}\left(\frac{\upsilon_L}{\upsilon_T}\right)^2\right]^2\right\}$	Magnitude of Burgurs vector	B_d [Å]	2
	Longitudinal phonon velocity of PbTe	υ_L [m/s]	3590
	Transverse phonon velocity of PbTe	υ_T [m/s]	1260
$\tau^{-1}{}_p = \upsilon(\sigma_s^{-1} + \sigma^{-1}{}_l)V_p$; $\sigma_s = 2\pi R^2$,	Average radius of nanoscale precipitates	R [nm]	2.25
	Mass density of PbTe	D_{PbTe}[kg/m^3]	8164
$\sigma_I = \pi R^2 \frac{4}{9}(\Delta D/D)^2 (\omega R/\Psi)^4$	Mass density of BaTe	D_{BaTe} [kg/m^3]	5130
	Number density of nanoscale precipitates	V_P [m^{-3}]	7.8578×10^{23}
$\tau_S^{-1} \approx \frac{144s\,\gamma^2\varepsilon_m^2 r_0^4}{\upsilon}\omega^2$	Misfit between the matrix and the precipitate	ε_0	0.07
$\tau^{-1}{}_{PD}$ (described in the text)	Phenomenological parameter of PbTe	E	65
	Mass of an atom Pb	M_{Pb} [amu]	207.2
	Te	M_{Te}	127.6
	Ba	M_{Ba}	137.33
	Radius of an atom Pb	r_{Pb}[pm]	175
	Te	r_{Te}	140
	Ba	r_{Ba}	222
	Fractional occupant	f_{Pb}	0.999
		f_{Te}	1
		f_{Ba}	0.001
	Degeneracy	c_1, c_2	1

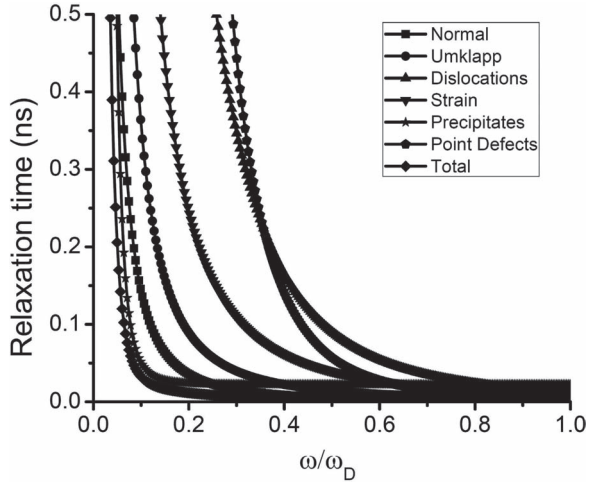

Figure 7. Relaxation time versus normalized frequency of PbTe-3% BaTe at 300 K.

conducted as following: heat up to 1323 K for 15 h, then hold for 10 h. The cooling was first down to 873 K at the rate of 11 K/h and then down to room temperature for 15 h.

Powder diffraction, thermal and electrical conductivity were conducted with an INEL diffractometer using Cu K_α radiation, NetzschLFA 457, and ULVACZEM, respectively. The thermal conductivity was calculated by $\kappa_{total} = \alpha C_P \delta$, where α is thermal diffusivity, C_P is heat capacity calculated relative to 9606 reference and δ is density of the specimen calculated by the mass and dimension.

Microanalysis was conducted under JEOL 2100F S/TEM with 200 kV. TEM samples were prepared by standard conventional method with polishing, dimpling, Ar-ion-milling with liquid nitrogen cooling stage. High-resolution image simulation was done by MacTempas computer code with input parameters: 2 mm for spherical aberration, 8 nm for defocus spread, 0.55 mrad for semi-convergence angle of illumination and 7 nm^{-1} for objective lens aperture diameter.

Supporting Information

Supporting Information is available from the Wiley Online Library or from the author.

Acknowledgements

This contribution is based on work supported as part of the Revolutionary Materials for Solid State Energy Conversion, an Energy Frontier Research Center funded by the U.S. Department of Energy, Office of Science, Office of Basic Energy Sciences under Award Number DE-SC0001054. Additional financial support from the Office of Naval Research is also gratefully acknowledged. Transmission electron microscopy work was performed in the (EPIC) (NIFTI) (Keck-II) facility of NU*ANCE* Center at Northwestern University. The NU*ANCE* Center is supported by NSF-NSEC, NSF-MRSEC, Keck Foundation, the State of Illinois, and Northwestern University.

Received: May 4, 2012
Revised: June 29, 2012
Published online: August 1, 2012

[1] G. J. Snyder, E. S. Toberer, *Nat. Mater.* **2008**, *7*, 105.
[2] M. G. Kanatzidis, *Chem. Mater.* **2010**, *22*, 648.
[3] M. S. Dresselhaus, G. Chen, M. Y. Tang, R. G. Yang, H. Lee, D. Z. Wang, Z. F. Ren, J. P. Fleurial, P. Gogna, *Adv. Mater.* **2007**, *19*, 1043.
[4] L. E. Bell, *Science* **2008**, *321*, 1457.
[5] J. P. Heremans, V. Jovovic, E. S. Toberer, A. Saramat, K. Kurosaki, A. Charoenphakdee, S. Yamanaka, G. J. Synder, *Science* **2008**, *321*, 554.
[6] A. I. Hochbaum, P. Yang, *Chem. Rev.* **2010**, *110*, 527.
[7] J. Tang, H.-T. Wang, D. H. Lee, M. Fardy, Z. Huo, T. P. Russell, P. D. Yang, *Nano Lett.* **2010**, *10*, 4279.
[8] K. F. Hsu, S. Loo, F. Guo, J. S. Dyck, C. Uher, T. Hogan, E. K. Polychroniadis, M. G. Kanatzidis, *Science* **2004**, *303*, 818.
[9] J. Androulakis, K. F. Hsu, R. Pcionek, H. Kong, C. Uher, J. J. D'Angelo, A. Downey, T. Hogan, M. G. Kanatzidis, *Adv. Mater.* **2006**, *18*, 1170.
[10] J. R. Sootsman, D. Y. Chung, M. G. Kanatzidis, *Angew. Chem. Int. Ed.* **2009**, *48*, 8616.
[11] J. He, J. Androulakis, M. G. Kanatzidis, V. P. Dravid, *Nano Lett.* **2012**, *12*, 343–347.
[12] K. Biswas, J. He, Q. Zhang, G. Wang, C. Uher, V. P. Dravid, M. G. Kanatzidis, *Nat. Chem.* **2011**, *3*, 160.
[13] P. F. P. Poudeu, J. D'Angelo, H. Kong, A. Downery, J. L. Short, R. Pcionek, T. P. Hogan, C. Uher, M. G. Kanatzidis, *J. Am. Chem. Soc.* **2006**, *128*, 14347.
[14] G. T. Alekseeva, B. A. Efimova, L. M. Ostrovskaya, O. S. Serebryannikova, M. I. Tsypin, *Sov. Phys. Semicond.* **1971**, *4*, 1122.
[15] S. N. Girard, J. He, C. Li, S. Moses, G. Wang, C. Uher, V. P. Dravid, M. G. Kanatzidis, *Nano Lett.* **2010**, *10*, 2825.
[16] J. He, S. N. Girard, M. G. Kanatzidis, V. P. Dravid, *Adv. Funct. Mater.* **2010**, *20*, 764.
[17] J. He, J. R. Sootsman, S. N. Girard, J.-C. Zheng, J. Wen, Y. Zhu, M. G. Kanatzidis, V. P. Dravid, *J. Am. Chem. Soc.* **2010**, *132*, 8669.
[18] L.-D. Zhao, S.-H. Lo, J. He, H. Li, K. Biswas, J. Androulakis, C.-I. Wu, T. P. Hogan, D.-Y. Chung, V. P. Dravid, M. G. Kanatzidis, *J. Am. Chem. Soc.* **2011**, *133*, 20476.
[19] S. Johnsen, J. He, J. Androulakis, V. P. Dravid, I. Todorov, D. Y. Chung, M. G. Kanatzidis, *J. Am. Chem. Soc.* **2011**, *133*, 3460.
[20] Y. Pei, A. LaLonde, S. Iwanaga, G. J. Snyder, *Energy Environ. Sci.* **2011**, *4*, 2085.
[21] K. Biswas, J. He, G. Wang, S.-H. Lo, C. Uher, V. P. Dravid, M. G. Kanatzidis, *Energy Environ. Sci.* **2011**, *4*, 4675.
[22] T. C. Harman, P. J. Taylor, M. P. Walsh, B. E. LaForge, *Science* **2002**, *297*, 2229.
[23] R. F. Egerton, *Electron energy-loss spectroscopy in the electron microscope*, Springer, New York **1996**.
[24] T. Kelly, T. Gribb, J. D. Olson, R. L. Martens, J. D. Shepard, S. A. Wiener, T. C. Kunicki, R. M. Ulfig, D. R. Lenz, E. M. Strennen, E. Oltman, J. H. Bunton, D. R. Stralit, *Microsc. Microanal.* **2004**, *10*, 373.
[25] I. Blum, I. Dieter, D. N. Seidman, J. He, J. Androulakis, K. Biswas, V. P. Dravid, M. G. Kanatzidis, *J. Electron. Mater.* **2012**, *41*, 1583.
[26] C. B. Lioutas, N. Frangis, I. Todorov, D. Y. Chung, M. G. Kanatzidis, *Crystals*, *Chem. Mater.* **2010**, *22*, 5630.
[27] S. Iwamura, M. Nakayam, Y. Miura, *Mater. Sci. Forum* **2002**, *396–402*, 1151.
[28] A. J. Porter, R. C. Ecob, R. A. Ricks, *J. Microscopy* **1983**, *129*, 327.
[29] D. B. Williams, C. B. Carter, *Transmission electron microscopy*, Springer, New York **2009**.
[30] M. J. Hÿtch, E. Snoeck, R. Kilaas, *Ultramicroscopy* **1998**, *74*, 131.
[31] J. Q. He, E. Vasco, C. L. Jia, R. H. Wang, *Appl. Phys. Lett.* **2005**, *87*, 062901.
[32] J. Callaway, *Phys. Rev.* **1959**, *113*, 1046.
[33] D. T. Morelli, J. P. Heremans, G. A. Slack, *Phys. Rev. B* **2002**, *66*, 195304.
[34] E. F. Steigmeier, B. Abeles, *Phys. Rev.* **1964**, *136*, A1149.
[35] J. Zou, D. Kotchetkov, A. A. Balandin, D. I. Florescu, F. H. Pollak, *J. Appl. Phys.* **2002**, *92*, 2534.
[36] W. Kim, A. Majumdar, *J. Appl. Phys.* **2006**, *99*, 084306.
[37] W. Kim, S. L. Singer, A. Majumdar, J. M. O. Zide, D. Klenov, A. C. Gossard, S. Stemmer, *Nano Lett.* **2008**, *8*, 2097.
[38] N. Mingo, D. Hauser, N. P. Kobayashi, M. Plissonnier, A. Shakouri, *Nano Lett.* **2009**, *9*, 711.
[39] B. Abeles, *Phys. Rev.* **1963**, *131*, 1906.
[40] J. Yang, G. P. Meisner, L. Chen, *Appl. Phys. Lett.* **2004**, *85*, 1140.
[41] M. Ohta, K. Biswas, S.-H. Lo, J. He, D. Y. Chung, V. P. Dravid, M. G. Kanatzidis, *Adv. Energy Mater.* DOI: 10.1002/aenm.201100756.